

Article

Thermodynamic Analysis of an Increasing-Pressure Endothermic Power Cycle Integrated with Closed-Loop Geothermal Energy Extraction

Hao Yu, Xinli Lu ^{*}, Wei Zhang and Jiali Liu

Department of Energy and Power Engineering, School of Mechanical Engineering, Tianjin University, Tianjin 300350, China; hao_yu@tju.edu.cn (H.Y.); zhang_wei@tju.edu.cn (W.Z.); jiali_liu@tju.edu.cn (J.L.)

* Correspondence: xinli.lu@tju.edu.cn

Abstract: The thermodynamic analysis of an increasing-pressure endothermic power cycle (IPEPC) integrated with closed-loop geothermal energy extraction (CLGEE) in a geothermal well at a depth from 2 km to 5 km has been carried out in this study. Using CLGEE can avoid some typical problems associated with traditional EGS technology, such as water contamination and seismic-induced risk. Simultaneous optimization has been conducted for the structural parameters of the downhole heat exchanger (DHE), the CO₂ mixture working fluid type, and the IPEPC operating parameters. The CO₂-R32 mixture has been selected as the optimal working fluid for the IPEPC based on the highest net power output obtained. It has been found that, when the DHE length is 4 km, the thermosiphon effect is capable of compensating for 53.8% of the pump power consumption. As long as the DHE inlet pressure is higher than the critical pressure, a lower DHE inlet pressure results in more power production. The power generation performance of the IPEPC has been compared with that of the organic Rankine cycle (ORC), trans-critical carbon dioxide cycle (t-CO₂), and single-flash (SF) systems. The comparison shows that the IPEPC has more net power output than other systems in the case that the DHE length is less than 3 km, along with a DHE outer diameter of 0.155 m. When the DHE outer diameter is increased to 0.22 m, the IPEPC has the highest net power output for the DHE length ranging from 2 km to 5 km. The application scopes obtained in this study for different power generation systems are of engineering-guiding significance for geothermal industries.

Keywords: theoretical study; increasing-pressure endothermic process; downhole heat exchanger; thermosiphon effect; CO₂-based mixture working fluid; geothermal power generation



Citation: Yu, H.; Lu, X.; Zhang, W.; Liu, J. Thermodynamic Analysis of an Increasing-Pressure Endothermic Power Cycle Integrated with Closed-Loop Geothermal Energy Extraction. *Energies* **2024**, *17*, 1756. <https://doi.org/10.3390/en17071756>

Academic Editors: Marija Macenić and Tomislav Kurevija

Received: 6 March 2024

Revised: 2 April 2024

Accepted: 5 April 2024

Published: 6 April 2024



Copyright: © 2024 by the authors. Licensee MDPI, Basel, Switzerland. This article is an open access article distributed under the terms and conditions of the Creative Commons Attribution (CC BY) license (<https://creativecommons.org/licenses/by/4.0/>).

1. Introduction

The need for fossil fuel-based energy has grown due to the world's expanding population and growing reliance on modern technology [1]. The extensive use of fossil fuels has led to many climate problems and much environmental pollution, which are constantly changing our living environment. In the last several decades, research has revealed that developing novel geothermal systems and improving the efficiency of geothermal systems currently being used are feasible options for tackling these difficulties [2]. Geothermal energy refers to the thermal energy that is naturally generated and stored within the Earth's subsurface. The estimated global geothermal energy resource is 600,000 EJ per annum according to the World Energy Assessment [3]. Geothermal energy is a sustainable and environmentally friendly resource that can be harnessed by numerous countries situated in geologically advantageous locations. As of the end of 2021, the global capacity for power generation from geothermal sources reached 15.85 GW. [4]. According to the World Geothermal Congress 2023 (WGC2023) held in Beijing, China, the world's total installed capacity of geothermal power generation has increased to 16.13 GW in 2022. The U.S., Indonesia, the Philippines, Turkey, and New Zealand (top 5 countries) have installed 3.79 GW, 2.36 GW, 1.94 GW, 1.68 GW, and 1.04 GW, respectively.

The geothermal utilization schemes depend on the types of resources available, including dry steam, hydrothermal, hot dry rock (HDR), geopressed, and magma [5]. Investigations show that HDR accounts for more than 90% of the U.S. geothermal resources. The Los Alamos National Laboratory pioneered the design and implementation of an enhanced geothermal system (EGS) prototype in the 1970s to effectively harness the energy stored in HDR [6]. The traditional EGS concept follows a straightforward approach: drilling production and injection wells; creating an artificial reservoir through hydrofracturing; connecting the injection and production wells for fluid circulation; and subsequently extracting heat from the geological formation. However, numerous practical challenges persist in EGS application, encompassing issues such as corrosion and scaling occurring in wellbores, the risk of water contamination, seismic-induced hazards, as well as working fluid loss during circulation [7,8]. To overcome these issues associated with current EGS technology, it is crucial to pursue a reliable and long-lasting heat extraction system along with an innovative power cycle for the effective utilization of hot dry rock resources.

Using a closed-loop geothermal energy extraction (CLGEE) is another way to extract heat from HDR, in which the working fluid (water or CO₂) does not contact the geof ormation [9]. Hodgson [10] first put forward the closed-loop concept in 192; since then, CLGEE has received more and more attention from researchers. The deep borehole or downhole heat exchanger (DBHE or DHE), installed to build the CLGEE and to extract the geothermal energy, usually has four types: co-axial case, inclined shaft, L-type, and U-type [11,12]. In terms of how to improve the heat extraction efficiency, the structure of the heat exchanger and the type of the working fluid are the key points of the CLGEE. The literature survey is also carried out according to these aspects, and the survey results are shown in Table 1.

Table 1. CLGEE studies reviewed in the literature.

Source	DHE Type	DHE Depth	Bottom Temperature	Working Fluid	Findings
Fox et al. (2016) [13]	Co-axial case	5.5 km	680 °C	sCO ₂	1 MW of power generation over 25 years of operation. A 100 m well spacing should be selected to avoid thermal interference.
Yildirim et al. (2019) [14]	Co-axial case; Multi-tube; U-type	2500 m	160 °C	R134a	The optimal mass flow rate for R134a is determined to be 64 kg/s with a net power output of 2511 kW; annual electricity generation is calculated as 20.89 GWh.
Amaya et al. (2020) [15]	Vertical tube-in-tube	330 m	180 °C	Water and sCO ₂	GreenFire Energy installed a demonstration closed-loop geothermal power generation system; tests show that the power output is up to 1.2 MW.
Yuan et al. (2021) [12]	U-type	1828.8 m	150 °C	Water	The heat exchange in vertical injection and production well is minimal compared with the 10-multilateral tube; the CLGEE can provide 9 to 11 MW of stable heat production over 30 years.

Table 1. Cont.

Source	DHE Type	DHE Depth	Bottom Temperature	Working Fluid	Findings
Beckers et al. (2022) [9]	Co-axial case; U-type	2–4 km	500 °C	Water and sCO ₂	The thermal output range for 2 km vertical co-axial is 0.4 to 0.9 MW, and that of 2 km U-type is 1.3 to 4.5 MW; Utilizing sCO ₂ as the working fluid to drive a turbine for electricity generation is more effective than using a water-driving turbine. The maximum heat transfer efficiency can be achieved at a mass flow rate of 40 kg/s under the condition of 3 branches and a horizontal tube length of 2000 m; The lowest power generation price is obtained under the condition of 4 branches and a 3000 m horizontal tube when the temperature is between 180 to 240 °C.
Wang et al. (2022) [16]	U-type with multi-level or multi-branch	3 km	200 °C	Water	The average output thermal power for 456 h from the geothermal system ranges from 172 kW to 262 kW based on the operating condition chosen, and the total thermal energy generated changes between 82 MWh and 194 MWh from a single borehole.
Pokhrel et al. (2022) [17]	Co-axial case	500 m	190 °C	Water	CO ₂ -based CLGEE produces two times more heating power than water-based CLGS when the working fluid is entirely driven by the thermosiphon effect.
Yu et al. (2023) [18]	Co-axial case in abandoned wells	3 km	146 °C	Water and sCO ₂	Ammonia, water, CO ₂ , isobutane, R41, R152a, R245fa, R32, and R134a were compared;
Dai et al. (2023) [19]	Co-axial case	1.8 km	57 °C	Ammonia, water, CO ₂ , R32 et al.	The ammonia has a relatively low inlet pressure (5 MPa) and pressure loss (2.7 MPa), which means ammonia has a lower circulation pump.
Liu et al. (2023) [20]	Co-axial case	2.6 km	175 °C	Water	A higher fluid capacity yields lower production temperature but higher thermal power; The tube's outer diameter has a limited effect on the thermal power efficiency.

The thermodynamic performance comparison among the CO₂ trans-critical Rankine cycle and ORC using R245fa has been carried out by Guo et al. [21]; the results indicate that the trans-critical Rankine cycle with CO₂ as the working fluid exhibits a 3–7% higher net power output and an 84% reduction in turbine inlet flow area. However, it necessitates the use of stronger materials and larger heat transfer areas. Although the thermal performance of CO₂ is better than water in DHE, the condensation of CO₂ into liquid at ambient temperature poses a significant challenge, impeding its widespread adoption and utilization in power cycles. However, the practical and most commonly used approach involves adding a second organic compound to CO₂ in order to form a mixture [22]. This CO₂-based fluid has a higher critical temperature than pure CO₂, which enables the use of a conventional condenser [23].

In the study of Pan et al. [24], R290 was added to CO₂ to solve the condensation problem; their study shows that when the mass fraction of R290 is higher than 0.24, the mixture can be condensed by conventional cooling water. Sánchez et al. [25] analyzed the technical and environmental effects of a trans-critical Rankine cycle with eight different CO₂-based mixtures; the obtained results show that mixtures with a high mass fraction of refrigerant tend to generate more net power than nearly pure CO₂ mixtures. The utilization of CO₂-based mixtures in a trans-critical power cycle could yield superior thermodynamic and economic performances compared to the use of pure CO₂, regardless of high or low temperatures; using R32-CO₂ as the working fluid has the highest exergy efficiency of 52.85% [26]. Guo et al. [27] proposed a comprehensive comparative method to investigate the impact of CO₂-based mixtures on the solar power tower plant in terms of power generation. In the study of Pan et al. [28], both the flammability of the mixture and the cycle performance have been considered for CO₂-n-butane and CO₂-isobutane: CO₂-isobutane has the highest thermal efficiency (12.97%) with a mole ratio of 0.72–0.28; the flammable critical mole ratios for CO₂-n-butane and CO₂-isobutane are 0.96–0.04 and 0.91–0.09, respectively. In our previous study [29], an increasing-pressure endothermic cycle was built for a geothermal artesian well. The findings indicate that the CO₂-based mixture exhibits a pronounced buoyancy-driven thermosiphon effect when subjected to gravitational potential energy, resulting in an outlet pressure of DHE higher than its inlet pressure.

The primary aim of the study is to develop a novel closed-loop geothermal power generation system for HDR. Despite research efforts placed on analyzing DHE with CO₂ or water as the working fluid, few studies have been oriented from integrated research on heat extraction in DHE and power generation. The quantitative analyses of the thermosiphon effect on CO₂-based mixtures are usually neglected in the large-scale DHE.

This study presents a novel cycle (increasing-pressure endothermic power cycle, IPEPC) for power generation using HDR resources, and the working fluids of the power cycle are CO₂-based mixtures, which undergo an endothermic process of increasing pressure within the DHE. The IPEPC system is a closed-loop system that does not require the extraction of geothermal fluids to surface equipment, and the working fluid does not contact the geo-formation directly, which can effectively avoid the problems caused by traditional EGS projects, such as corrosion and scaling occurring in wellbores, water contamination, and seismic-induced hazards. More importantly, in traditional EGS projects, the fractures formed by the hydraulic fracturing technique usually become narrower and narrower, resulting in a decline in mass flow rate or even zero flow rate after a long-term operation. In contrast, the IPEPC system does not have such problems and can run stably for a long time.

The above-ground power generation unit and under-ground DHE were treated as one whole for conducting an integrated research study on IPEPC. Differing from the hundreds-of-meters-long DHE used by Amaya et al. [15], in our study, the thermosiphon effect of CO₂-based mixtures in the thousands-of-meters-long DHE is quantitatively analyzed. The effects of the CO₂-based mixtures, DHE structural size, DHE inlet pressure, and working fluid mass flow rate on IPEPC power generation performance are investigated under the geothermal conditions of 2 km to 5 km depth.

2. Geothermal Power Generation Systems

2.1. Description of the IPEPC

The schematic diagram of the investigated increasing-pressure endothermic power cycle (IPEPC) is depicted in Figure 1a, while Figure 1b illustrates the temperature–entropy (T-s) diagram of the IPEPC. The IPEPC is a trans-critical geothermal power generation system, consisting of a power generation unit (above-ground section) and a downhole heat exchanger (DHE) used for the closed-loop heat extraction.

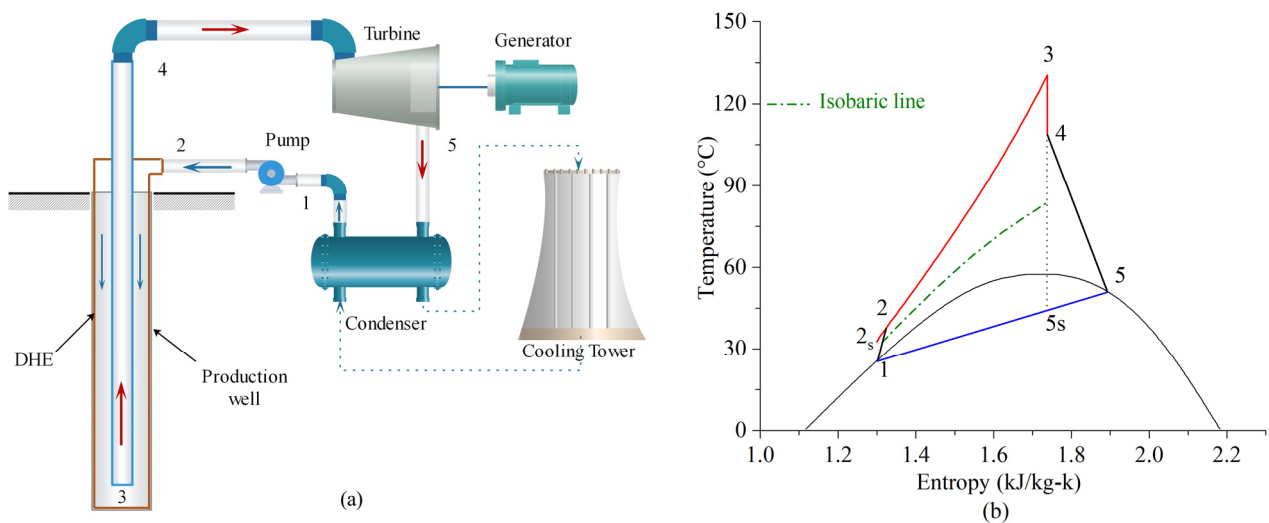


Figure 1. Schematic diagram (a) and the temperature–entropy diagram (b) of the IPEPC.

In the IPEPC, a CO₂-based mixture is used as the working fluid. The working fluid undergoes pressurization to reach a supercritical state (process 1–2). Subsequently, it is injected into the annular conduit of the DHE. The downward flow within this annulus effectively absorbs heat from the surrounding geological formations, as depicted in Figure 1b (process 2–3). The outer pipe is connected to the inner pipe at the bottom section. Within the inner pipe, the working fluid ascends from the bottom to the top (process 3–4), undergoing a progressive decrease in pressure and temperature. Subsequently, the working fluid derived from DHE enters the turbine to generate electricity (process 4–5). The exhaust of the turbine (state 5) is directed into the condenser, where it undergoes condensation, thereby transforming into a fully saturated liquid (state 1).

The process 2–4 (red line) is an endothermic process with increasing pressure, which differs from the working fluid evaporation in a conventional ORC. The green dash–dot line is an isobaric line in the traditional ORC system; it can be seen that the outlet temperature and pressure of the isobaric endothermic process are significantly lower than that of the DHE outlet (state 4). The thermosiphon effect can enhance the outlet working fluid pressure of the DHE by leveraging the disparity in density between the downward and upward pipes, thereby leading to an improvement in power generation performance for IPEPC.

2.2. Description of the Trans-Critical Carbon Dioxide (t-CO₂) System

The schematic diagram of the t-CO₂ system is identical to that of the IPEPC system, with the only distinction being the utilization of pure CO₂ as the working fluid instead of a CO₂-based mixture. Notably, the condensation process in this system occurs at a constant temperature without any temperature glide.

2.3. Description of the Organic Rankine Cycle (ORC) System

The schematic diagram of the ORC investigated in this study is shown in Figure 2a. The water from the evaporator is pressurized into an over-pressured state (process 1–2) and is then injected into the annular conduit of the DHE, where it flows downward in the annulus and absorbs heat from the rock formation, as described in process 2–3. The water that extracted heat then passes upward from the bottom to the top (process 3–4) in the DHE inner pipe, and the water from the DHE is fed into the evaporator to heat the circulation working fluid of ORC (process 4–1). The working fluid from the evaporator is directed into the turbine to generate electricity (process 5–6). Subsequently, the exhaust from the turbine (state 6) is channeled into the condenser where it undergoes condensation, transitioning into a fully liquid phase (state 7), and is then pressurized through the pump to its evaporation pressure (process 7–8). Then, another cycle starts.

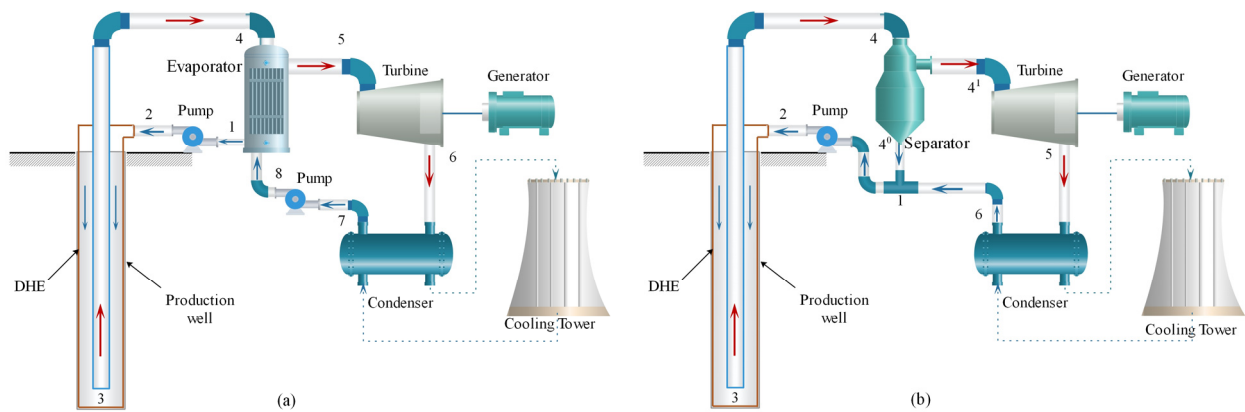


Figure 2. Schematic diagrams of the ORC (a) and the SF (b).

2.4. Description of the Single-Flash (SF) System

The schematic diagram of the SF system investigated in this study is shown in Figure 2b. In the SF system, water is used as the working fluid. Hot water from the DHE goes into the separator and is separated into vapor (state 4¹) and liquid (state 4⁰). The vapor from the separator flows into the turbine to generate electricity (process 4¹–5). The turbine exhaust is condensed by cooling water in the condenser (process 5–6), then the liquid from the separator and the condenser is mixed and injected into the DHE by the pump.

3. Methodology and Models

The study only considers one-dimensional radial heat transfer, due to the concentricity of the production well and co-axial DHE. The aspects included in the DHE heat transfer model are as follows: between the geological formation and the DHE outer pipe, and between the outer pipe and the inner pipe of the DHE. The diagram of the production well and the DHE are illustrated in Figure 3, showing the incorporation of adiabatic material within the thermal insulation layer to ensure effective heat preservation between the inside wall and the outside wall. The models of t-CO₂, ORC, and SF have been comprehensively reviewed and explained by Yu et al. [4] and Guo et al. [21], so they are not extensively discussed here.

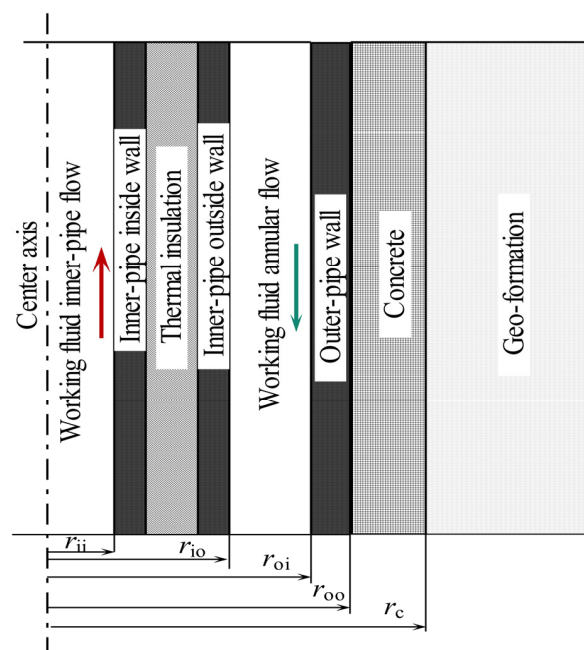


Figure 3. Schematic diagram of the DHE model.

3.1. Solution Procedure and Assumptions

Figure 4 shows the flow chart of the IPEPC model solution procedure.

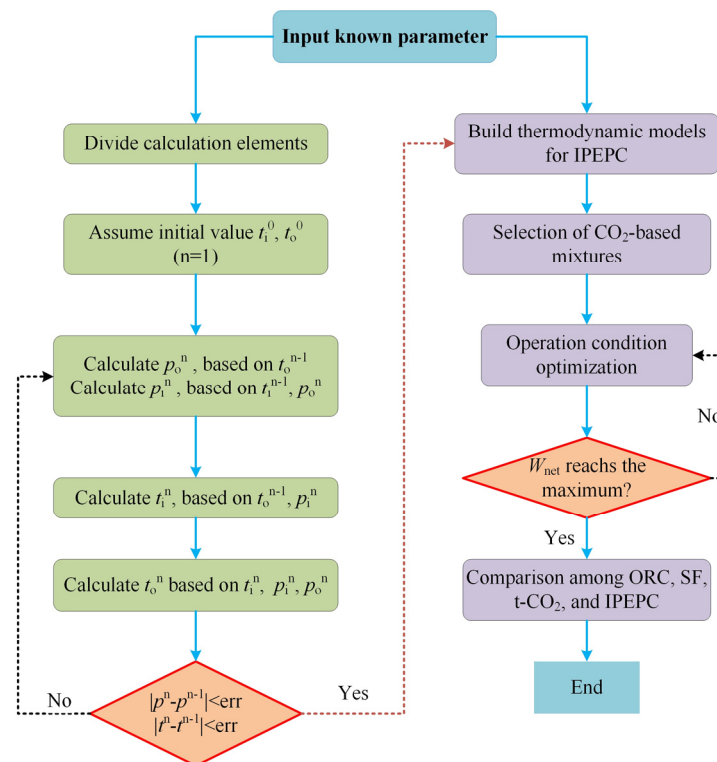


Figure 4. Flow chart of the IPEPC model solution procedure.

The simulation process was conducted based on the following assumptions:

1. The four systems are all operating in a stable state;
2. The flow friction and heat losses in pipes are disregarded in the ground power generation equipment;
3. The CO₂-based mixture is in a saturated liquid state at the condenser outlet;
4. The geothermal gradient of the geo-formation remains constant, the temperature increases linearly with depth;
5. The turbine and pump efficiencies, as well as the temperature of the cooling water, remain consistent across all four systems;
6. A 20% increase in net power generation is the criterion by which IPEPC, ORC, and SF systems are superior to t-CO₂, which aligns with the requirements of our ongoing sponsored project.

The numerical simulation was performed on Engineering Equation Solver (EES, Version 10), and all the transport and thermodynamic parameters of the cycle fluids (pure and mixtures) were computed based on the REFPROP 10 database from the National Institute of Standards and Technology (NIST) [30]. Due to the presence of temperature glide, the zeotropic mixtures are capable of effectively matching both the cold and hot sources during the condensation process [25,31]. The working fluids selected for this study are CO₂-based mixtures. The selection for organic working fluid (OWF) has taken into account thermal properties, environmental sustainability, flammability, and toxicity. Based on the literature survey and our previous study [23,29,32], four organic working fluids (R161, R32, R152a, and R1234yf) commonly used in power generation units were investigated in this study. Table 2 shows the thermal-physical properties of the CO₂ and four organic working fluids used in this article.

Table 2. Properties of the investigated working fluids [29,32].

Substance	Critical Temperature (T_c , °C)	Critical Pressure (P_c , MPa)	ODP	GWP	Atmospheric Life (Years)	ASHRAE Class
CO ₂	30.98	7.38	0	1	200	A1
R32	78.1	5.78	0	675	4.9	A2
R1234yf	94.7	3.38	0	4.4	0.029	A2L
R161	102.2	5.09	0	12	0.21	A3
R152a	113.3	4.52	0	124	1.4	A2

The working fluids employed in this study all possess an ASHRAE class A classification, which signifies the highest level of safety [33]. The simulation employed the parameters listed in Table 3.

Table 3. Parameters used in the simulation model.

Items	Parameters
Isentropic efficiency of turbine, η_t	0.85
Isentropic efficiency of pump, η_p	0.8
Condenser outlet temperature, T_{co} (°C)	25
Cooling water temperature, T_{ci} (°C)	20
Inner pipe inside diameter, d_{ii} (m)	0.083
Inner pipe outside diameter, d_{io} (m)	0.10
Annulus pipe inside diameter, d_{oi} (m)	0.135
Annulus pipe outside diameter, d_{oo} (m)	0.155
Well casing diameter, d_c (m)	0.178
Rock formation density, ρ_e (kg/m ³)	2650
Rock heat capacity, c_e (J/kg·k)	837
Rock formation thermal conductivity, λ_e (W/m·k)	2.5
Well casing thermal conductivity, λ_{ca} (W/m·k)	30
Insulated tube thermal conductivity, λ_{ins} (W/m·k)	0.02
Cement thermal conductivity, λ_{ce} (W/m·k)	0.72
Geothermal gradient, grad T (°C/km)	40

3.2. Power Generation Model

The power generation system comprises a turbine, condenser, and working fluid pump.

3.2.1. Turbine

According to Figure 1, the turbine generator power output can be determined using the following equation:

$$W_g = m_m(h_4 - h_{5s})\eta_t = m_m(h_4 - h_5) \quad (1)$$

where W_g is the system's power generation (kW); η_t is the turbine isentropic efficiency, m_m is the working fluid mass flow rate (kg/s); h is the fluid's specific enthalpy (kJ/kg); and the subscripts 4 and 5 are the turbine inlet and outlet states.

3.2.2. Condenser

The condensation process (5–1 in Figure 1) of the CO₂-based mixture is non-isothermal with a temperature glide, resulting in an improved alignment of temperature changes between the cooling water and the working fluid, thereby reducing heat transfer irreversibility. The condensation pressure is equal to the turbine outlet pressure, and the heat balance in the condenser is given as follows:

$$Q_c = m_m(h_5 - h_1) \quad (2)$$

where Q_c is the heat exchanged in the condensation process (kW).

3.2.3. Working Fluid Pump

The working fluid pump power consumption is given as follows:

$$W_p = m_m(h_2 - h_1) \quad (3)$$

The net power generation is the difference between total power generation and pump power consumption:

$$W_{\text{net}} = W_g - W_p \quad (4)$$

where W_p is the working fluid pump power consumption (kW) and W_{net} is the net power output (kW).

3.3. Downhole Heat Exchanger (DHE) Model

Differing from the above-ground evaporator, the heat transfer calculation procedure of working fluids in the DHE took the effect of the gravity field into account. The temperature and velocity of CO₂-based mixtures are interconnected and resolved through the coupling of energy, momentum, and mass equations. Variations in flow velocity affect temperature due to friction losses and the Joule–Thomson effect. Therefore, all these factors must be taken into account in the simulation.

3.3.1. DHE Flow Pressure Model

The CO₂-based mixtures are considered compressible and simplified as one-dimensional flow. The simulation procedure is under steady conditions and calculated using the finite difference method. The mass and momentum equations were simplified as follows [34]:

$$\frac{d}{dz}(\rho v) = 0 \quad (5)$$

$$\frac{d}{dz}(\rho v^2) = -\frac{dp}{dz} \pm \rho g - \frac{\tau_w \pi d}{A_p} \quad (6)$$

On combining Equations (5) and (6), the working fluid pressure expression is as follows:

$$\frac{dp}{dz} = \pm \rho g - \rho v \frac{dv}{dz} - f \frac{\rho v^2}{2d} \quad (7)$$

where ρ represents the working fluid density (kg/m³); v represents the velocity of working fluid (m/s); z represents the flow path coordinate (m); g represents the gravitational acceleration (m/s²); P represents the working fluid pressure (Pa); τ_w represents the shear stress (MPa); d represents the equivalent diameter (m); A_p represents the cross-sectional area (m²); “+” and “−” indicate whether the flow direction is aligned or opposed to the gravitational acceleration; and f represents the Darcy friction factor, proposed by Wang et al. [35].

3.3.2. DHE Flow Temperature Model

The energy equation can be given as follows:

$$\frac{d}{dz} \left[\rho v \left(h + \frac{1}{2} v^2 \right) \right] = -\frac{d}{dz}(\rho v) \pm \rho v g - \frac{q}{A_p} \quad (8)$$

On combining Equations (5) and (8), the energy conservation equation can be written as follows:

$$\frac{dh}{dz} = \pm g - v \frac{dv}{dz} - \frac{q}{m} \quad (9)$$

where q is the heat flow rate per meter (W/m).

The “ h ” equation can be written as follows [36]:

$$\frac{dh}{dz} = c_p \frac{dT}{dz} - \mu_{J-T} c_p \frac{dp}{dz} \quad (10)$$

where c_p is the working fluid-specific heat capacity (J/kg·K) and μ_{J-T} represents the Joule–Thomson coefficient (K/Pa).

Substituting Equation (9) into Equation (10), the working fluid temperature has another expression:

$$\frac{dT}{dz} = -\frac{q}{mc_p} + \frac{1}{c_p} \left(\mu_{J-T} c_p \frac{dp}{dz} \pm g - v \frac{dv}{dz} \right) \quad (11)$$

3.3.3. DHE Heat Transfer Model

The heat transfer model encompasses the following aspects: heat transfer between the surrounding geological formation and DHE, as well as heat transfer between the outer and inner pipes. The overall heat flow rate can be given by:

$$q = \pi d U \Delta T \quad (12)$$

(a) Heat transfer between the inner and outer pipe

The inner pipe is composed of three parts: an inside wall, an insulation layer, and an outside wall. The heat transfer can be described as follows:

$$R_{io} = \frac{1}{2\pi r_{ii} h_i} + \frac{1}{2\pi \lambda_i} \ln\left(\frac{r_{iil}}{r_{ii}}\right) + \frac{1}{2\pi \lambda_{ins}} \ln\left(\frac{r_{io1}}{r_{iil}}\right) + \frac{1}{2\pi \lambda_o} \ln\left(\frac{r_{io}}{r_{io1}}\right) + \frac{1}{2\pi r_{io} h_o} \quad (13)$$

$$U_{io} = \frac{1}{2\pi r_{iil} R_{io}} \quad (14)$$

where R_{io} represents the thermal resistance between the inner and outer pipes (K/W); r_{ii} and r_{iil} represent the inner pipe’s inside wall inner radius and outer radius (m); r_{io1} and r_{io} represent the inner pipe’s outside wall inner radius and outer radius (m); λ_i , λ_o , and λ_{ins} represent the inside wall, outside wall, and insulation layer’s heat conductivities (W/m²·K); h_i and h_o represent the inner and outer pipe’s convective heat transfer coefficients (W/m²·K); and U_{io} represents the heat transfer coefficient between the inner and outer pipes (W/m²·K).

(b) Heat transfer between the geological formation and outer pipe

$$R_{ow} = \frac{1}{2\pi r_{oi} h_o} + \frac{1}{2\pi \lambda_o} \ln\left(\frac{r_{oo}}{r_{oi}}\right) + \frac{1}{2\pi \lambda_c} \ln\left(\frac{r_c}{r_{oo}}\right) \quad (15)$$

$$U_{ow} = \frac{1}{2\pi r_{oi} R_{ow}} \quad (16)$$

where R_{ow} is the thermal resistance between the well casing and outer pipe (K/W); r_{oi} and r_{oo} are the outer pipe’s inner and outer radii (m); r_c is the outer radius of the well casing (m); λ_o and λ_c are the outer pipe and well casing heat conductivity (W/m²·K); and U_{ow} denotes the heat transfer coefficient between the well casing and outer pipe (W/m²·K).

3.4. Model Verification

The results of this study were compared with those of Yu et al. [18] in order to validate the accuracy of the model. In the comparative study, water and CO₂ were chosen as working fluids, and the geothermal gradient of 25–45 °C/km was taken into account. In their study, a geothermal heat pump model (with a coefficient of performance of 3.5) was built for building heating, and T2Well was used for DHE heat extraction calculation. In this software, only the diameter of DHE is set and the pipe thickness is ignored. The

rock permeability is very small, and it is regarded as a compact rock without water. The parameters of the numerical model are shown in Table 4.

Table 4. Parameters used in the comparative study [18].

Items	Parameters
Well depth, km	3
Rock density, kg/m ³	2570
Heat conductivity, W/m·K	1.8
Surface temperature, °C	12
Rock permeability, m ²	1.5×10^{-15}
DHE inner radius, mm	65
DHE outer radius, mm	100
Wellbore wall heat conductivity, W/m·K	2.5
Insulation layer heat conductivity, W/m·K	0.02
Working fluid inlet temperature, °C	10
CO ₂ wellhead pressure, MPa	7.5
Water wellhead pressure, MPa	0.1013

Under the same numerical conditions as the study conducted by Yu et al. [18], Figure 5 illustrates the heat power of CO₂ and water with respect to different geothermal gradients. The blue line and red line represent the CO₂ and water results reported by Yu et al., respectively. The discrepancy between the CO₂ simulation results obtained from the IPEPC model and those reported by Yu et al. [18] is 1.78%; whereas for water, it is 1.97%. Consequently, considering the acceptable difference in heat power between the reference and simulation results, we can conclude that the IPEPC model demonstrates accuracy.

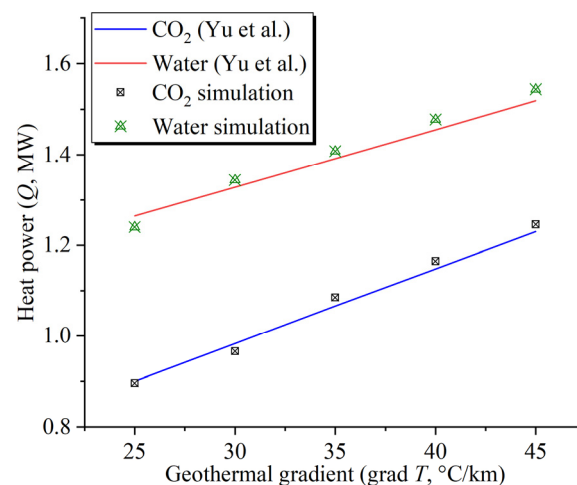


Figure 5. Heat power comparison between the IPEPC model and the model proposed by Yu et al. [18].

4. Results and Discussion

This section presents the optimization results of the IPEPC system, including the selection of CO₂-based mixtures, the optimization of the DHE inlet pressure, and the analysis of the matching relationship between the DHE diameter and the working fluid mass flow rate. Based on the thermodynamic analysis, the net power outputs of IPEPC, ORC, SF, and t-CO₂ were compared.

4.1. CO₂-Based Mixture Selection

The variations in the DHE outlet pressure (P_{out}) in response to different mass flow rates (m_m) and CO₂-based mixtures are illustrated in Figure 6. The DHE lengths (L) investigated are 2 km, 3 km, 4 km, and 5 km. The DHE inlet pressure (P_{in}) is maintained at 8 MPa.

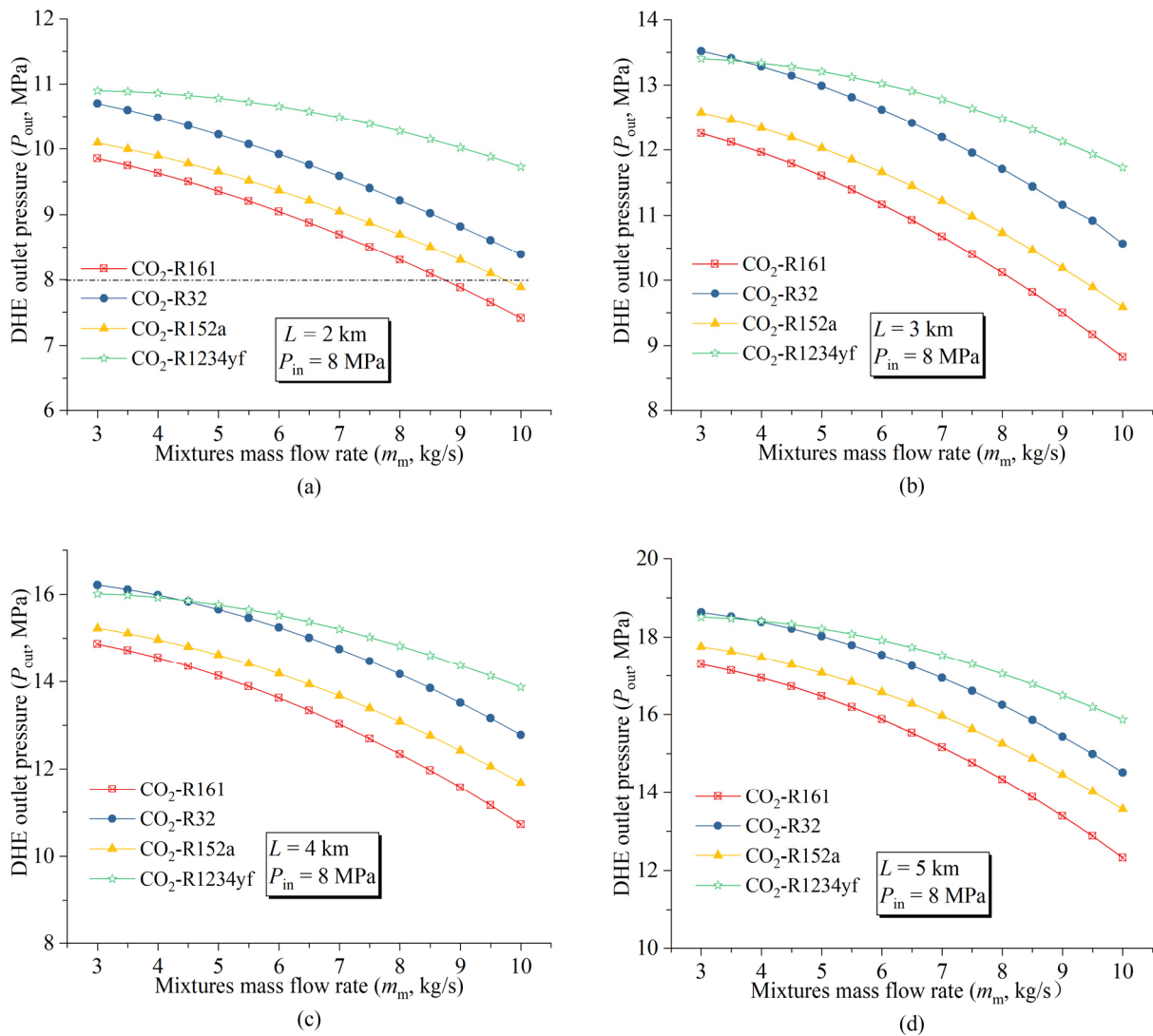


Figure 6. Effect of the working fluid flow rates on the DHE output pressures with respect to different CO₂-based mixture working fluids (mass fraction: OWF/CO₂ = 0.5/0.5, $d_{oo} = 0.155$ m): (a) $L = 2$ km; (b) $L = 3$ km; (c) $L = 4$ km; and (d) $L = 5$ km.

When the DHE length (L) is 2 km (Figure 6a), the DHE outlet pressure (P_{out}) of each working fluid decreases with an increase in its mass flow rate m_m and the P_{out} of CO₂-R1234yf is higher than that of other mixtures. The horizontal line (black dash-dot) represents the DHE inlet pressure (P_{in}). Any pressure variations in P_{out} above this line suggest the presence of the thermosiphon effect, whereby gravitational potential energy enables P_{out} to exceed the corresponding P_{in} within a certain range of mass flow rates m_m . Due to the thermosiphon effect's ability to offset pump power consumption ($P_{out} > P_{in}$), the turbine experiences an increased inlet pressure, resulting in an enhanced power generation performance.

It can be seen that the P_{out} of all the mixture working fluids involved is higher than the P_{in} when the L is higher than 2 km (Figure 6b–d). The thermosiphon effect of the four mixtures can be ranked from high to low: CO₂-R1234yf > CO₂-R32 > CO₂-R152a > CO₂-R161.

The variations in IPEPC net power output (W_{net}) in response to different m_m and CO₂-based mixtures are illustrated in Figure 7. When the L is 2 km (Figure 7a), each mixture exhibits an optimal m_m that maximizes the W_{net} . The utilization of CO₂-R1234yf as the IPEPC working fluid yields the highest W_{net} (27.3 kW for $m_m = 7.5$ kg/s), slightly surpassing

that achieved by selecting CO₂-R32 as the working fluid (26.2 kW for $m_m = 6$ kg/s); CO₂-R161 and CO₂-R152a are the two mixtures with poor power generation performances for IPEPC at the shallow depth. In the case that the L is 3 km (Figure 7b), the W_{net} curve of CO₂-R32 moves to the top and has the highest value (100.2 kW for 9 kg/s). The W_{net} curve of CO₂-R161 converges towards that of CO₂-R32, ranking as the second highest.

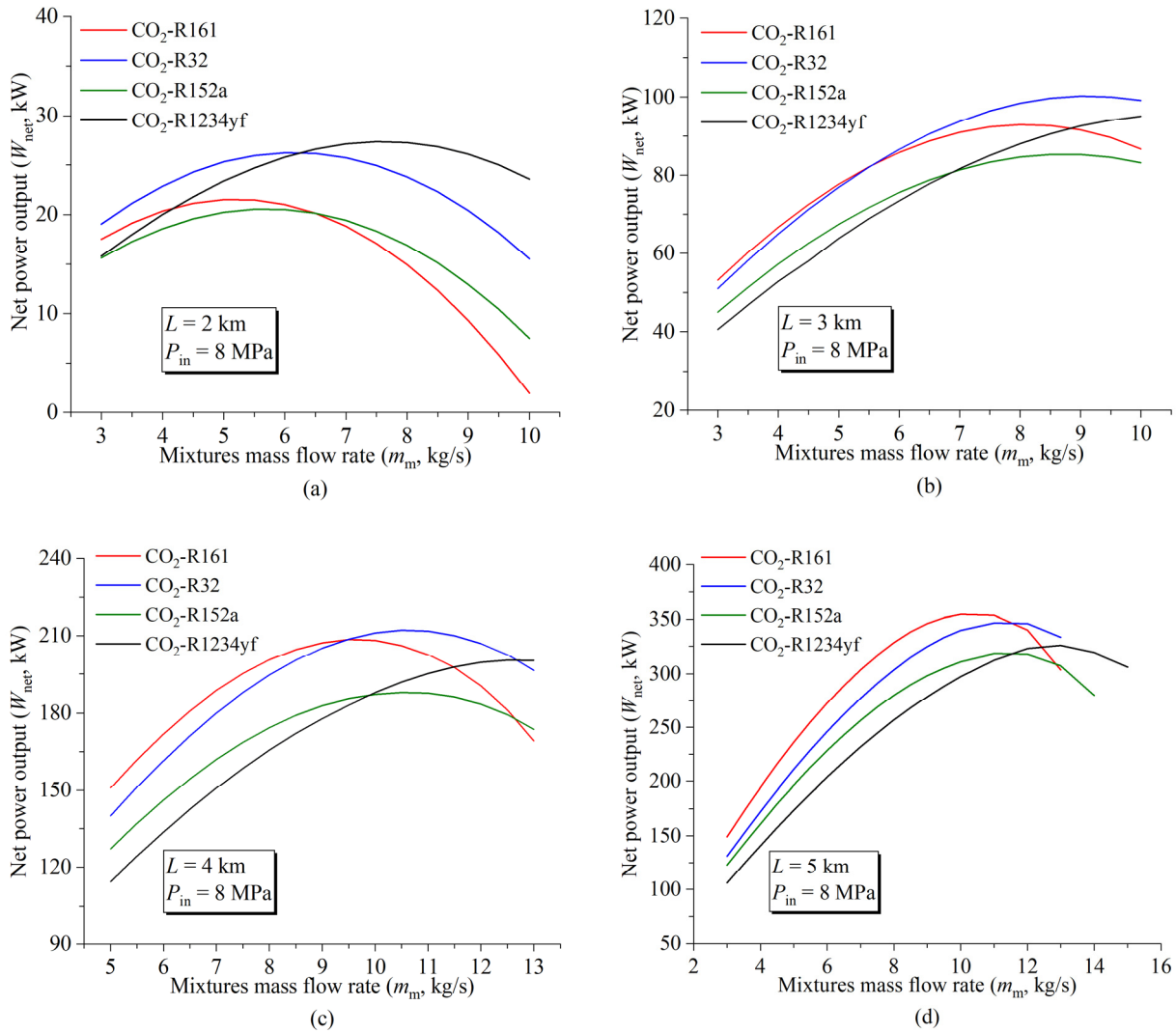


Figure 7. Effect of the working fluid flow rates on net power outputs with respect to different CO₂-based mixture working fluids (mass fraction: OWF/CO₂ = 0.5/0.5, $d_{oo} = 0.155$ m): (a) $L = 2$ km; (b) $L = 3$ km; (c) $L = 4$ km; and (d) $L = 5$ km.

In the case that the L is 4 km (Figure 7c), the W_{net} curve of CO₂-R161 becomes the highest within a wide mass flow rate range ($m_m < 9.5$ kg/s). When the mass flow rate is higher than 9.5 kg/s, the IPEPC system with CO₂-R32 as the working fluid has the highest net power output (212.2 kW). It can also be noted that the net power output of the four mixtures can be ranked from high to low: CO₂-R161 > CO₂-R32 > CO₂-R1234yf > CO₂-R152a, under the condition that the L is high (5 km; Figure 7d). Considering that using CO₂-R32 as the working fluid of the IPEPC has the highest net power output under most geothermal conditions, and that R32 is cheaper than R161, CO₂-R32 was selected as the working fluid for the performance analyses of the IPEPC in the following sections.

Figure 8 shows the effect of CO₂-R32 mass flow rate and R32 mass fraction on the net power output (W_{net}) for four DHE length (L) conditions (2 km, 3 km, 4 km, and 5 km), with the DHE inlet pressure (P_{in}) maintained at 8 MPa. When the DHE is shallow (2 km;

Figure 8a), the maximum net power output for each mass flow rate is achieved at a mass fraction value of 0, indicating that pure CO₂ should be utilized under these geothermal conditions to optimize power generation performance.

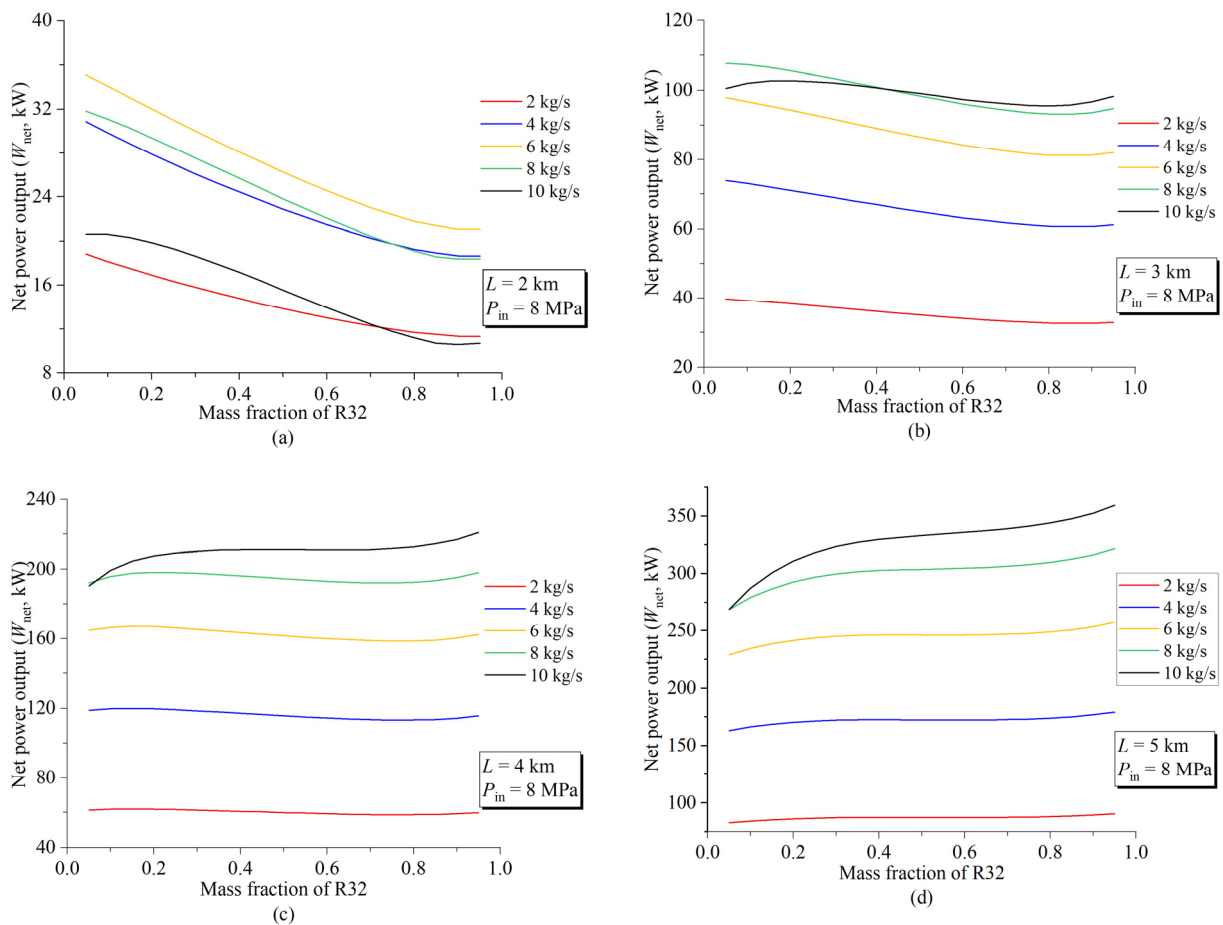


Figure 8. IPEPC net power output variations with respect to R32 mass fraction for different CO₂-R32 mass flow rates ($d_{oo} = 0.155$ m): (a) $L = 2$ km; (b) $L = 3$ km; (c) $L = 4$ km; and (d) $L = 5$ km.

The optimal mass fraction shifts towards higher values as the length of DHE increases. Taking $m_m = 10$ kg/s as an example, the optimal values of the mass fractions of R32/CO₂ are 0.2/0.8 and 1/0 for the DHE length of 3 km (Figure 8b) and 4 km (Figure 8c), respectively. It is also worth pointing out that the increase in W_{net} is almost negligible after the mass fraction of R32 continues to increase from 0.3 to 0.8.

Under the condition that the DHE L is high (5 km; Figure 8d), a pure organic working fluid would be a more optimal choice in each scenario; as illustrated in Figure 8d, each curve reaches its peak at a mass fraction of 1.

Table 5 shows the impact of the thermosiphon effect on the pump's power consumption under two different DHE conditions (3 km, 4 km). When the DHE length is 2 km, the inlet pressure for DHE is determined to be 8 MPa, resulting in an outlet pressure of 11.16 MPa due to the presence of the thermosiphon effect. In a traditional subcritical ORC, the maximum outlet pressure of the working fluid from the evaporator cannot exceed its inlet pressure. By comparing Scenario 1 and Scenario 2 as presented in Table 5, the impact of the thermosiphon effect on pump power consumption can be determined. In Scenario 1, with the CO₂-R32 pressurized to 8 MPa, the pump's power consumption amounts to 55.1 kW; in Scenario 2, with the CO₂-R32 pressurized to 11.16 MPa, the pump's power consumption reaches 97.2 kW. The thermosiphon effect can offset a significant portion of the pump's power consumption by compensating for 42.1 kW, which accounts for approximately 43.3% of the total pump power consumed. When considering a DHE length of 4 km,

the thermosiphon effect is capable of compensating for an even higher amount of pump power consumption at approximately 71.4 kW or around 53.8% of the total pump power.

Table 5. Pump power consumption compensated by the thermosiphon effect (working fluid: CO₂-R32).

Equipment	Items	DHE: 3 km		DHE: 4 km	
		CO ₂ -R32 = 0.5–0.5, 9 kg/s		CO ₂ -R32 = 0.5–0.5, 10 kg/s	
		Inlet	Outlet	Inlet	Outlet
Pump working Scenario 1	$T, ^\circ\text{C}$	25	29.79	25	29.79
	P, MPa	4	8	4	8
	$h, \text{kJ/kg}$	253.9	260.02	253.9	260.02
	W_{p1}, kW		55.1		61.2
DHE	P, MPa	8	11.16	8	12.78
Pump working Scenario 2	P, MPa	As Pump 1	11.16	As Pump 1	12.78
	$h, \text{kJ/kg}$	As Pump 1	264.7	As Pump 1	267.16
	W_{p2}, kW		97.2		132.6
	Pump power consumption difference	$W_{p2} - W_{p1}$ $(W_{p2} - W_{p1})/W_{p2} \times \%$		42.1 43.3%	

4.2. Effect of the DHE Inlet Pressure and Mixture Mass Flow Rate

The impact of the mixture mass flow rate (m_m) and DHE inlet pressure (P_{in}) on the net power output (W_{net}) is illustrated in Figure 9. Reducing the P_{in} can effectively increase the W_{net} of the IPEPC, indicating that the pressure loss of CO₂-R32 in the DHE flow process can be compensated by the thermosiphon effect without a reduction in W_{net} instead. The large-scale DHE acts as both a heat exchanger and a booster pump. When the P_{in} is constant, the W_{net} increases at first and then decreases. The existence of an optimal m_m that maximizes the W_{net} is observed; as the value of L increases, so does the value of the optimal m_m . (9 kg/s for 3 km; 10 kg/s for 4 km).

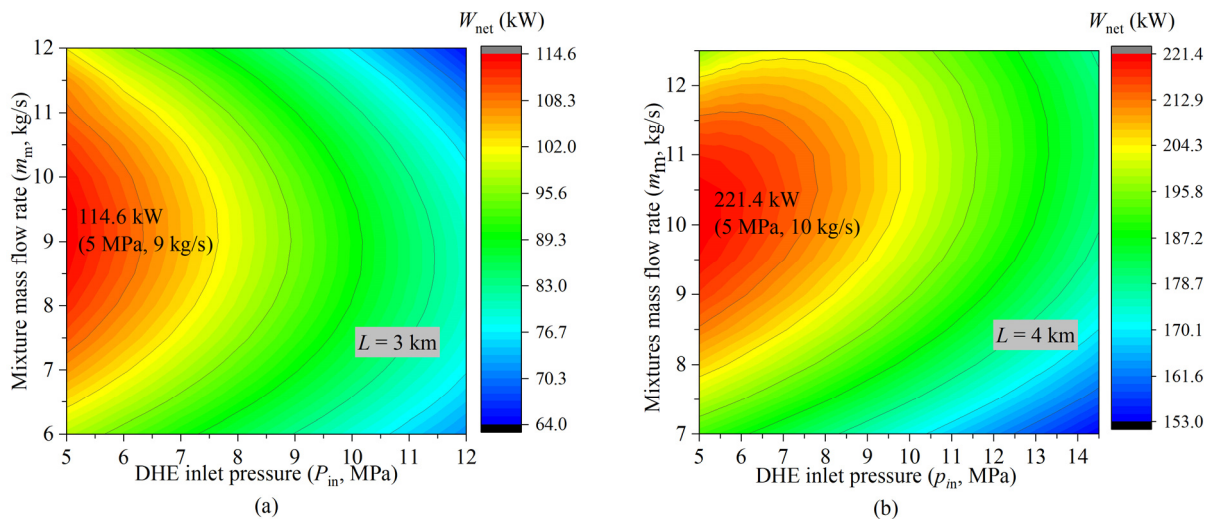


Figure 9. Net power output tendency with respect to different m_m and P_{in} (mass fraction of R32/CO₂ = 0.5/0.5): (a) $L = 3$ km and (b) $L = 4$ km.

4.3. Matching Relationship between the Mass Flow Rate and Pipe Diameter

The variations in the IPEPC net power output (W_{net}) with respect to the mixture mass flow rate (m_m) and the outside diameter of the outer pipe (d_{oo}) are illustrated in Figure 10. In Figure 10a ($L = 2000$ m), there exists an optimal m_m value that corresponds to the maximum W_{net} for each given d_{oo} . As can be seen in Figure 10a, when the d_{oo} is low ($d_{oo} = 0.145$ m), the optimal m_m is 5 kg/s, as shown by point A; when the d_{oo} is less than 0.195 m, the

optimal m_m is shown by line AB, indicating that there is an approximately linear matching relationship between the outer pipe's outside wall diameter and the optimal working fluid mass flow rate.

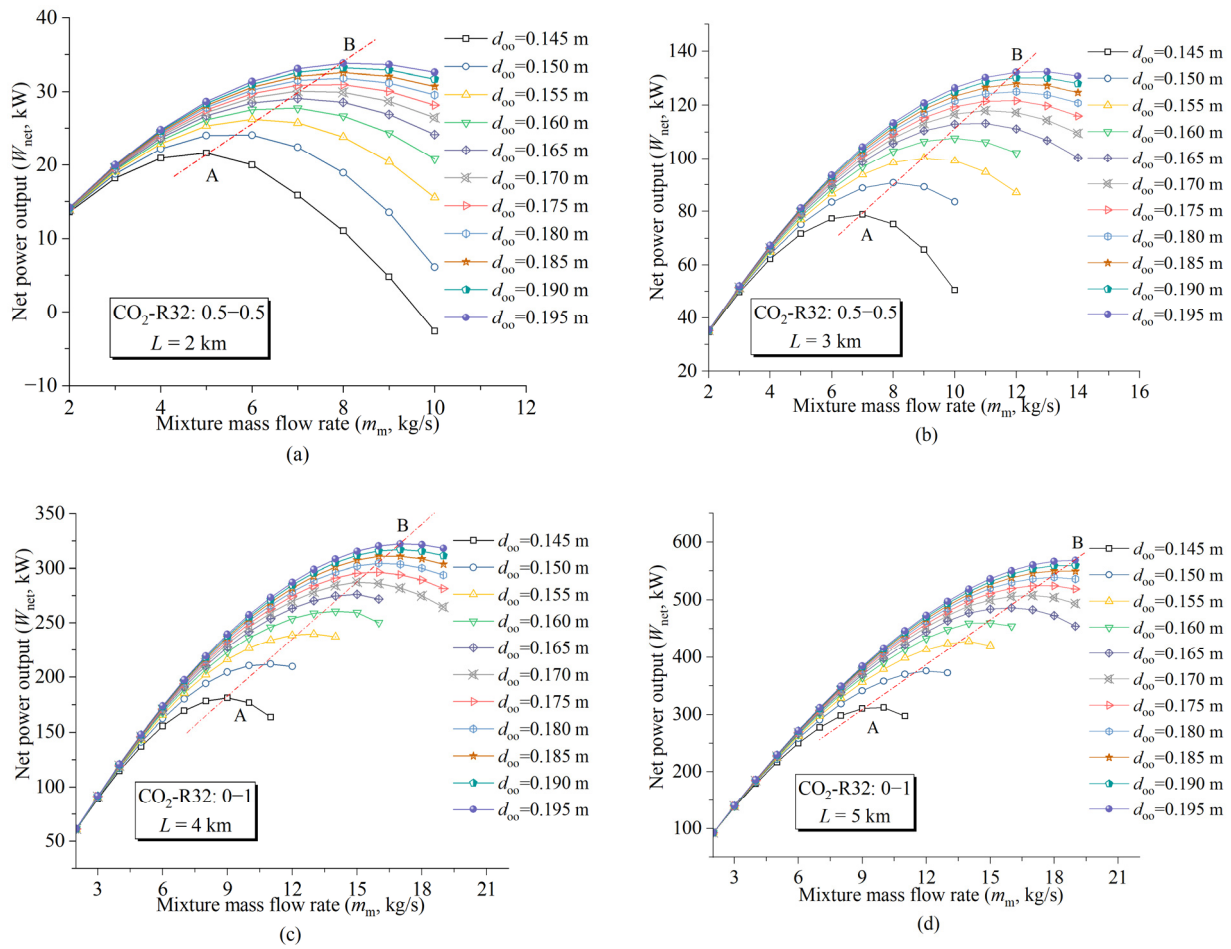


Figure 10. Net power output variations with respect to different m_m and d_{oo} ($P_{in} = 8$ MPa): (a) $L = 2$ km; (b) $L = 3$ km; (c) $L = 4$ km; and (d) $L = 5$ km.

When the L is higher, the corresponding optimal m_m is higher for each d_{oo} . It can be seen in Figure 10b that the optimal m_m for $d_{oo} = 0.145$ m is 7 kg/s (point A) and the optimal m_m for $d_{oo} = 0.195$ m is 12 kg/s (point B). It is also worth noting that the optimal m_m difference for point A and point B (m_{AB}) increases with the increase in DHE L ; the m_{AB} is 3 kg/s, 5 kg/s, 8 kg/s, and 10 kg/s when the L is 2 km, 3 km, 4 km, and 5 km, respectively.

On the other hand, there is an approximately linear relationship between the maximum W_{net} and the optimal m_m , as can be seen from line AB in Figure 10. When the L is 2 km (Figure 10a), the W_{net} of point A is 21.6 kW; the W_{net} of point B is 33.8 kW; the net power output difference for points A and B (W_{AB}) is 12.2 kW. The W_{net} difference for points A and B widens with the increase in L : the W_{AB} is 53.4 kW, 141.4 kW, and 256.7 kW when the L is 3 km, 4 km, and 5 km, respectively. The matching relationship between the pipe diameter and the working fluid mass flow rate has a great influence on the net power generation of IPEPC; hence, the results of this study are very important for the promotion and application of IPEPC.

4.4. Comparison among ORC, SF, t-CO₂, and IPEPC

The W_{net} comparisons among the ORC system, SF system, t-CO₂ system, and IPEPC system, considering different outer pipe outside diameters (d_{oo}) and DHE lengths (L), are illustrated in Figure 11. The comparisons have been conducted based on the optimal operation conditions achieved by each of the four systems. R245fa is employed as the working fluid for ORC, while CO₂-R32 is selected as the IPEPC working fluid.

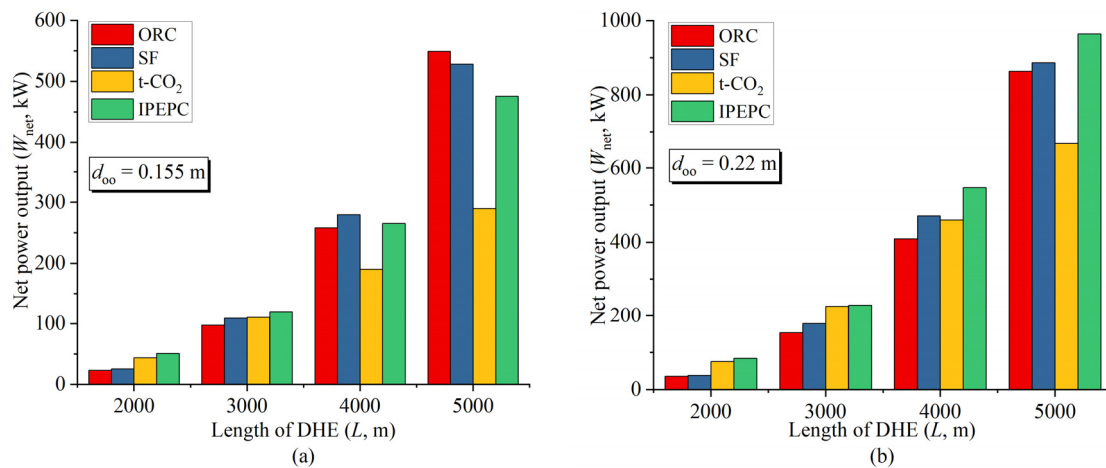


Figure 11. Net power output comparisons among four geothermal power generation systems with respect to different DHE lengths (L) and outer diameters (d_{oo}): (a) $d_{\text{oo}} = 0.155$ m and (b) $d_{\text{oo}} = 0.22$ m.

Figure 11a shows the comparison of the outer pipe's small outside diameters ($d_{\text{oo}} = 0.155$ m). When the L is 2 km, the W_{net} of the IPEPC surpasses that of the t-CO₂, SF, and ORC by 17.5%, 98.4%, and 120%, respectively; whereas it only exhibits an improvement of 7.4%, 9.1%, and 21.7% when the L extends to 3 km. For an L of 4 km, the SF system exhibits the highest W_{net} , while the t-CO₂ system demonstrates the poorest power generation performance. When the L extends to 5 km, the ORC surpasses SF as the leading system in terms of power generation performance.

When the outer pipe's outside diameter (d_{oo}) expands to 0.22 m, the W_{net} comparison is shown in Figure 11b. For an L of 2 km, the W_{net} of the IPEPC surpasses that of the t-CO₂, SF, and ORC by 11.8%, 124%, and 138%, respectively. However, if the L increases to 3 km, these improvements reduce to only 1.6%, 28.4%, and 49.3%. When the L is 4 km, the SF system has more net power output than the t-CO₂ system; meanwhile, the ORC system has the worst power generation performance. When the L is 5 km, the t-CO₂ replaced the ORC as the system with the worst net power generation performance. The net power output of IPEPC is 44.2%, 8.7%, and 11.7% higher than that of the t-CO₂, SF, and ORC, respectively.

It is worth noticing that the bigger the d_{oo} , the wider range of the L in which the IPEPC system shows more advantages over other systems on power generation.

Comparisons of the DHE outlet–inlet pressure difference (ΔP) among the four systems (ORC, SF, t-CO₂, and IPEPC), considering different outer pipe outside diameters (d_{oo}) and DHE lengths (L) are illustrated in Figure 12. Here, the outlet–inlet pressure difference (ΔP) is defined as the outlet pressure minus the inlet pressure. The comparisons have been conducted in the same manner as described in the previous section, based on the premise that each of the four systems has achieved its optimal operational condition.

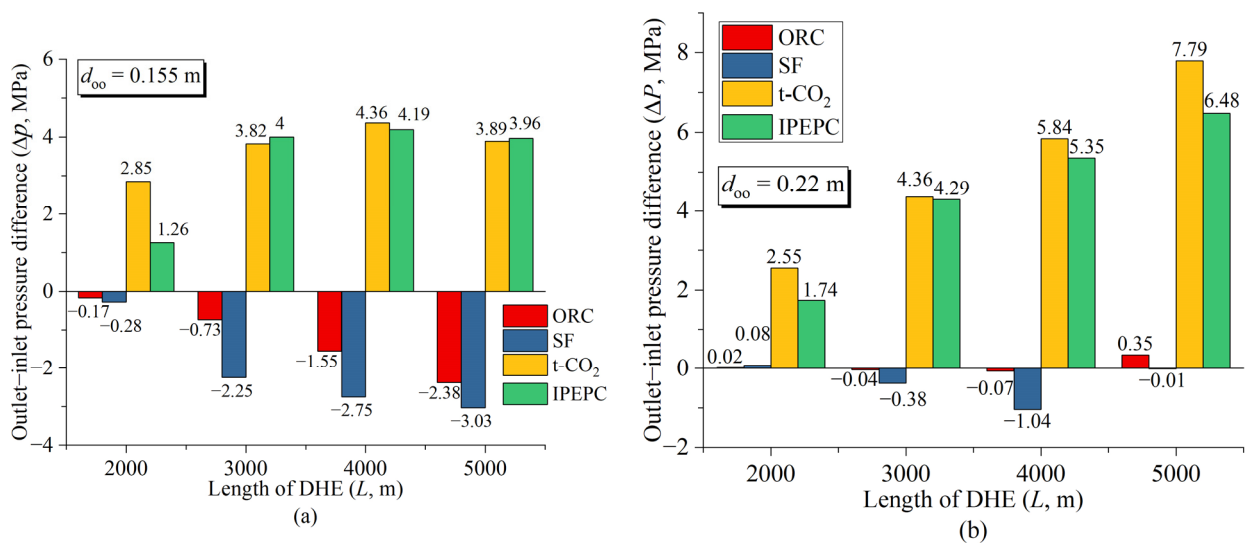


Figure 12. DHE outlet–inlet pressure difference comparisons among the four systems (ORC, SF, t-CO₂, and IPEPC) with respect to different DHE lengths (L) and outer diameters (d_{oo}): (a) $d_{oo} = 0.155$ m and (b) $d_{oo} = 0.22$ m.

Under the condition of small outer pipe outside diameters ($d_{oo} = 0.155$ m, see Figure 12), the DHE outlet–inlet pressure difference (ΔP) of the ORC and SF systems are always negative for each L . The absolute value of ΔP increases with the increase in the DHE length, indicating that the gravitational potential energy acting on water is ineffective, resulting in the absence of any noticeable thermosiphon effect. As the DHE depth increases, there is a greater pressure loss caused by flow friction resistance. Conversely, both t-CO₂ and IPEPC systems consistently display a positive ΔP for each L , suggesting that utilizing CO₂ or CO₂-based mixtures as working fluids in DHE has a distinct thermosiphon effect which leads to a reduced pump power consumption.

When the outer pipe’s outside diameter (d_{oo}) expands to 0.22 m, the comparison of the DHE outlet–inlet pressure difference is illustrated in Figure 12b. As the cross-sectional area increases, the pressure loss caused by flow friction resistance decreases accordingly. The DHE outlet–inlet pressure difference (ΔP) for both the ORC and SF systems is smaller compared to that shown in Figure 12a. For an L of 2 km, the ΔP values for the ORC and SF systems are no longer negative, indicating that the increase in pressure due to the thermosiphon effect slightly exceeds the pressure loss caused by flow friction resistance. The ΔP values for the t-CO₂ and IPEPC systems remain positive and higher than those depicted in Figure 12a when $L > 2$ km, suggesting that a larger d_{oo} generally results in a more significant thermosiphon effect.

Two selection maps generated to show the range of application for each system under different geothermal gradients (25 °C/km \leq grad $T \leq 55$ °C/km) and DHE lengths (2 km $\leq L \leq 5$ km) are shown in Figure 13. R245fa is the working fluid of ORC, while the DHE has two outer pipe outside diameters (0.155, 0.22 m). The t-CO₂ system was chosen as the reference system, a 20% net power output increment is the criterion by which the t-CO₂ system is permitted to be replaced by one of the other systems (IPEPC, SF, or ORC).

When the DHE outer pipe’s outside wall is 0.155 m (Figure 13a), the selection map consists of three scopes divided by the following lines: the red line (dashed), and the black line (solid). When the DHE length (L) is 2 km, the geothermal gradient (grad T) maximum value for using IPEPC is 41 °C/km. When the DHE length becomes 3 km, the geothermal gradient maximum value decreases to 35 °C/km. In the case that the DHE length is 4 km, the geothermal gradient maximum value is about 42.5 °C/km; when the DHE length is 5 km, the geothermal gradient maximum value decreases to 30 °C/km. The results presented in Figure 13a indicate that, when the geothermal gradient is relatively high and the DHE length is relatively low (below the black solid line), the IPEPC, SF, and

ORC systems are unable to achieve a net power increase of 20% compared to the t-CO₂ system. If the DHE length exceeds the threshold indicated by the black line, it is advisable to opt for the ORC system. The absence of the SF system in this selection map does not indicate its inability to generate 20% more W_{net} than the t-CO₂ system; rather, it is due to the fact that both the IPEPC and ORC systems have a higher capacity for power generation.

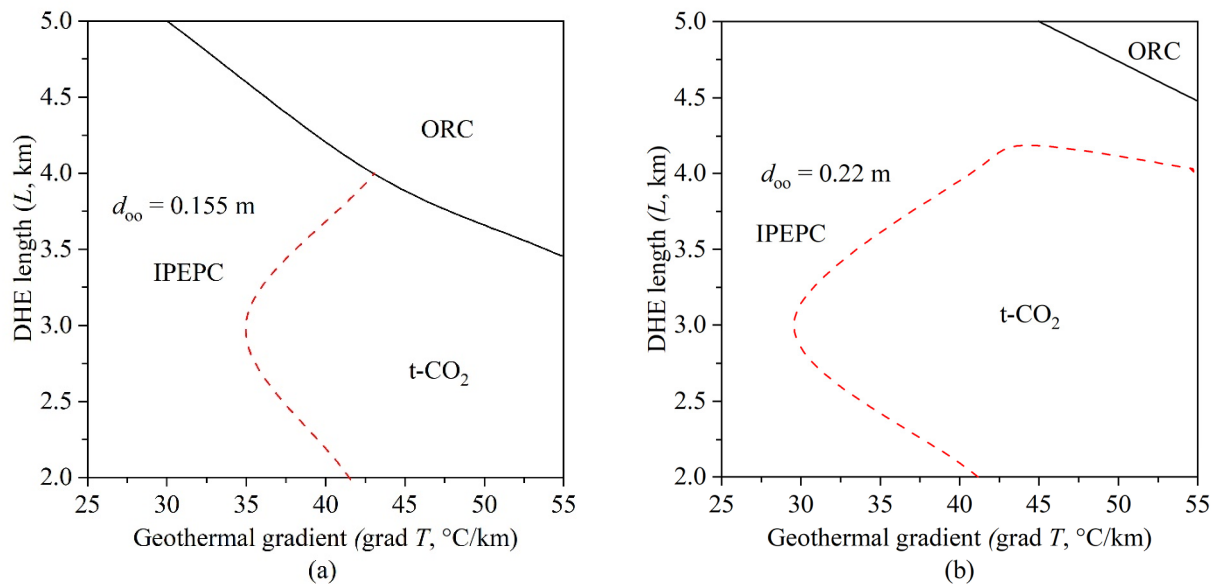


Figure 13. Application scopes of the three investigated systems: (a) $d_{\text{oo}} = 0.155$ m; (b) $d_{\text{oo}} = 0.22$ m.

When the DHE outer pipe's outside diameter increases to 0.22 m (Figure 13b), the selection map is still three regions and does not contain the application scope of the SF system. When the DHE length is 3 km, the application scope of the t-CO₂ system expands to the lower geothermal gradient (30 °C/km). It is worth noting that the application scope of the IPEPC system becomes wider when the DHE length is high (4–5 km); the application scope of the ORC system can only be narrowed to a very small area in the upper right corner.

5. Further Study

The performance of the IPEPC has been analyzed thermodynamically in this study. Further investigation is considered necessary for engineering application. Apart from the theoretical analysis, problems faced in the practical application should be investigated in detail as well. The economic performance, environmental impacts, and long-term operation performance of the IPEPC system will be the focus of the future study. In addition, field experiments are also needed to verify the increasing-pressure endothermic process.

6. Conclusions

An innovative IPEPC system integrated with closed-loop geothermal energy extraction has been established. A DHE is used for heat extraction from a geothermal well with a depth ranging from 2 km to 5 km. The influences of several key factors on the power generation performance of the IPEPC have been investigated. The key factors investigated in this study are the CO₂-based mixture composition, the mass flow rate, the mass fraction, the inlet pressure of DHE, and the matching relationship between the mixture mass flow rate and the DHE outer pipe's outside diameter. The influence of the thermosiphon effect on pump power consumption has also been analyzed quantitatively. In addition, comparisons among the ORC, t-CO₂, SF, and IPEPC systems in terms of the power generation and DHE outlet–inlet pressure difference have been made as well. The results obtained from this study can be concluded as follows:

- (1) The IPEPC model using a CO₂-based mixture as the working fluid has been developed, which can utilize a wide range of geothermal resources, including hot dry rock geothermal energy. The IPEPC, with a CO₂-R32 mixture as its working fluid, demonstrates an advantage over the other three power generation systems (t-CO₂, SF, and ORC).
- (2) It is shown that the power generation performance of the IPEPC can be enhanced by choosing a DHE inlet pressure slightly higher than the condensation pressure. The analysis of the thermosiphon effect indicates that the IPEPC system can achieve energy savings of 43.3% and 53.8% in pump power consumption corresponding to a DHE length of 3 km and 4 km, respectively.
- (3) There is an approximately linear matching relationship between the outer pipe's outside wall diameter and the optimal mass flow rate of the working fluid.
- (4) An IPEPC with a smaller outer pipe outside diameter ($d_{oo} = 0.155$ m) shows an advantage over the other three systems (t-CO₂, SF, and ORC) in terms of net power outputs only when the DHE length (L) is less than or equal to 3 km. In the case that the DHE length is 2 km, the net power output of IPEPC surpasses that of the t-CO₂, SF, and ORC by 17.5%, 98.4%, and 120%, respectively.
- (5) An IPEPC with a larger outer pipe outside diameter ($d_{oo} = 0.22$ m) shows an advantage in power generation over the other three systems (t-CO₂, SF, and ORC) for a wider range of the DHE length (ranging from 2 km to 5 km). In the case that the DHE length is 5 km, the net power output of IPEPC surpasses that of the t-CO₂, SF, and ORC by 44.2%, 8.7%, and 11.7%, respectively.
- (6) The DHE outlet–inlet pressure difference (ΔP) of either IPEPC or t-CO₂ system is positive for any given DHE length ranging from 2 km to 5 km, indicating that the DHE outlet pressure is greater than the inlet pressure if the IPEPC or t-CO₂ system is applied. This thermosiphon effect increases with the increase in DHE length for the system with a larger diameter ($d_{oo} = 0.22$ m). In contrast, the DHE outlet pressure is less than the inlet pressure in most cases if the ORC or SF system is applied.
- (7) The generated application scopes for the three investigated systems (IPEPC, t-CO₂, and ORC) show that the IPEPC always has an advantage over the t-CO₂ and ORC systems when the geothermal gradient is 30 °C/km or less. The greater the geothermal gradient and the longer the DHE, the more tendency is to use the ORC; however, a larger geothermal gradient alone can increase the tendency of using the t-CO₂ system. Increasing the outer pipe's outside diameter (d_{oo}) from 0.155 m to 0.22 m results in a larger application scope of the t-CO₂ system but a smaller scope of the ORC system.

Author Contributions: Conceptualization, H.Y. and X.L.; methodology, H.Y.; software, H.Y.; validation, H.Y., X.L. and J.L.; formal analysis, W.Z.; investigation, J.L.; resources, X.L.; data curation, W.Z.; writing—original draft preparation, H.Y.; writing—review and editing, X.L.; visualization, H.Y.; supervision, X.L.; project administration, X.L.; funding acquisition, X.L. and W.Z. All authors have read and agreed to the published version of the manuscript.

Funding: This research was funded by the Ministry of Science and Technology of China, grant number 2018YFB1501805.

Data Availability Statement: The data are contained within the article.

Acknowledgments: We thank the anonymous reviewers and editors for their comments and suggestions.

Conflicts of Interest: The authors declare no conflicts of interest.

Nomenclature

h	Specific enthalpy, kJ/kg	R_{i_o}	Total thermal resistance in DHE, K/W
L	DHE length, m	U_{i_o}	Overall heat transfer coefficient in DHE, W/m ² ·K
m_m	CO ₂ mixture mass flow rate, kg/s	R_{o_w}	Thermal resistance between wellbore and outer pipe, K/W
W_g	Turbine-generated power output, kW	U_{o_w}	Overall heat transfer coefficient between wellbore and outer pipe, W/m ² ·K
W_p	Pump consumed power, kW	z	Vertical coordinate, m
W_{net}	Net power output, kW	f	Friction factor
Q	Heat transfer rate, kW	d	Diameter, m
P_{in}	DHE inlet pressure, MPa	q	Heat flux per unit length, W/m
P_{out}	DHE outlet pressure, MPa	C_p	Heat capacity at constant, J/kg·K
P_c	Critical pressure, MPa	μ_{j-T}	Joule–Thomson coefficient, K/MPa
T_{in}	DHE inlet temperature, °C	A_p	Flow area, m ²
T_{out}	DHE outlet temperature, °C	λ_i	Inner pipe conductivity, W/m·K
T_c	Critical temperature, °C	λ_c	Well casing thermal conductivity, W/m·K
T_e	Formation temperature, °C	λ_{ins}	Insulated pipe thermal conductivity, W/m·K
T_w	Wellbore outside wall temperature, °C	λ_o	Outer pipe conductivity, W/m·K
η_t	Turbine isentropic efficiency, %	Abbreviations	
η_p	Pump isentropic efficiency, %	DHE	Downhole heat exchanger
d_{ii}	Inner pipe inside wall diameter, m	IPEC	Increasing-pressure endothermic cycle
d_{i_o}	Inner pipe outside wall diameter, m	ORC	Organic Rankine cycle
d_{o_i}	Outer pipe inside wall diameter, m	SF	Single-flash system
d_{o_o}	Outer pipe outside wall diameter, m	t-CO ₂	Trans-critical CO ₂ cycle
d_c	Well casing diameter, m	OWF	Organic working fluid
ρ_e	Density of rock, kg/m ³	HDR	Hot dry rock
τ_w	Shear stress, MPa	EGS	Enhanced geothermal system
v	Fluid velocity, m/s	ODP	Ozone depletion potential
g	Gravitational acceleration, m/s ²	GWP	Global warming potential
		CLGEE	Closed-loop geothermal energy extraction

References

- Budiono, A.; Suyitno, S.; Rosyadi, I.; Faishal, A.; Ilyas, A.X. A Systematic Review of the Design and Heat Transfer Performance of Enhanced Closed-Loop Geothermal Systems. *Energies* **2022**, *15*, 742. [\[CrossRef\]](#)
- Sharmin, T.; Khan, N.R.; Akram, M.S.; Ehsan, M.M. A State-of-the-Art Review on Geothermal Energy Extraction, Utilization, and Improvement Strategies: Conventional, Hybridized, and Enhanced Geothermal Systems. *Int. J. Thermofluids* **2023**, *18*, 100323. [\[CrossRef\]](#)
- Goldemberg, J. *World Energy Assessment Report: Energy and the Challenge of Sustainability*; United Nations Pubns: New York, NY, USA, 2000.
- Yu, H.; Lu, X.; Ma, F.; Zhang, W.; Liu, J.; Li, C. A study on geothermal electricity systems for Tibet geothermal fields considering thermal performance, economic analysis, and CaCO₃ scaling. *J. Renew. Sustain. Energy* **2023**, *15*, 013901. [\[CrossRef\]](#)
- Xu, C.; Dowd, P.A.; Tian, Z.F. A simplified coupled hydro-thermal model for enhanced geothermal systems. *Appl. Energy* **2015**, *140*, 135–145. [\[CrossRef\]](#)
- Huang, W.; Cao, W.; Jiang, F. A novel single-well geothermal system for hot dry rock geothermal energy exploitation. *Energy* **2018**, *162*, 630–644. [\[CrossRef\]](#)
- Breede, K.; Dzebisashvili, K.; Liu, X.; Falcone, G. A systematic review of enhanced (or engineered) geothermal systems: Past, present and future. *Geotherm. Energy* **2013**, *1*, 4. [\[CrossRef\]](#)
- Baek, H.; Chung, J.B.; Yun, G.W. Differences in public perceptions of geothermal energy based on EGS technology in Korea after the Pohang earthquake: National vs. local. *Technol. Forecast. Soc. Chang.* **2021**, *172*, 121027. [\[CrossRef\]](#)
- Beckers, K.F.; Rangel-Jurado, N.; Chandrasekar, H.; Hawkins, A.J.; Fulton, P.M.; Tester, J.W. Techno-Economic Performance of Closed-loop Geothermal Systems for Heat Production and Electricity Generation. *Geothermics* **2022**, *100*, 102381. [\[CrossRef\]](#)
- Hodgson, J.L. Examination of the problem of utilizing the Earth's internal heat. In Proceedings of the Section G of the British Association for the Advancement of Science at Its Leeds Meeting, Nottingham, UK, 2 September 1927.
- Kohl, T.; Brenni, R.; Eugster, W. System performance of a deep borehole heat exchanger. *Geothermics* **2002**, *31*, 687–708. [\[CrossRef\]](#)
- Yuan, W.; Chen, Z.; Grasby, S.E.; Little, E. Closed-loop geothermal energy recovery from deep high enthalpy systems. *Renew. Energy* **2021**, *177*, 976–991. [\[CrossRef\]](#)

13. Fox, D.; Higgins, B.; Energy, G.; Emeryville, C.A. The effect of well density on resource depletion for a vertical closed-loop sCO₂ Geothermal Well System. *Geotherm. Resour. Counc. Trans.* **2016**, *40*. Available online: <https://www.greenfireenergy.com/> (accessed on 4 April 2024).
14. Yildirim, N.; Parmanto, S.; Akkurt, G.G. Thermodynamic assessment of downhole heat exchangers for geothermal power generation. *Renew. Energy* **2019**, *141*, 1080–1091. [[CrossRef](#)]
15. Amaya, A.; Scherer, J.; Muir, J.; Patel, M.; Higgins, B. GreenFire Energy Closed-Loop Geothermal Demonstration using Supercritical Carbon Dioxide as Working Fluid. In Proceedings of the 45th Workshop on Geothermal Reservoir Engineering, Stanford, CA, USA, 10–12 February 2020.
16. Wang, G.; Ma, H.; Liu, S.; Yang, D.; Xu, X.; Fu, M.; Jia, H. Thermal power extraction from a deep, closed-loop, multi-level, multi-branch, U-shape borehole heat exchanger geothermal system. *Renew. Energy* **2022**, *198*, 894–906. [[CrossRef](#)]
17. Pokhrel, S.; Sasmito, A.P.; Sainoki, A.; Tosha, T.; Tanaka, T.; Nagai, C.; Ghoreishi-Madiseh, S.A. Field-scale experimental and numerical analysis of a downhole coaxial heat exchanger for geothermal energy production. *Renew. Energy* **2022**, *182*, 521–535. [[CrossRef](#)]
18. Yu, Y.; Cheng, F.; Cheng, J.; Yang, G.; Ma, X. Comparative thermo-economic analysis of co-axial closed-loop geothermal systems using CO₂ and water as working fluids. *Appl. Therm. Eng.* **2023**, *230*, 120710. [[CrossRef](#)]
19. Dai, J.; Li, J.; Wang, T.; Zhu, L.; Tian, K.; Chen, Z. Thermal performance analysis of coaxial borehole heat exchanger using liquid ammonia. *Energy* **2023**, *263*, 125986. [[CrossRef](#)]
20. Liu, S.; Taleghani, A.D. Factors affecting the efficiency of closed-loop geothermal wells. *Appl. Therm. Eng.* **2023**, *222*, 119947. [[CrossRef](#)]
21. Guo, T.; Wang, H.; Zhang, S. Comparative analysis of CO₂-based transcritical Rankine cycle and HFC245fa-based subcritical organic Rankine cycle using low-temperature geothermal source. *Sci. China* **2010**, *53*, 1638–1646. [[CrossRef](#)]
22. Garg, G.; Kumar, P.; Srinivasan, K.; Dutta, P. Evaluation of carbon dioxide blends with isopentane and propane as working fluids for organic Rankine cycles. *Appl. Therm. Eng.* **2013**, *52*, 439–448. [[CrossRef](#)]
23. Dai, B.; Li, M.; Ma, Y. Thermodynamic analysis of carbon dioxide blends with low GWP (global warming potential) working fluids-based trans-critical Rankine cycles for low-grade heat energy recovery. *Energy* **2014**, *64*, 942–952. [[CrossRef](#)]
24. Pan, L.; Wei, X.; Shi, W. Performance analysis of a zeotropic mixture (R290/CO₂) for trans-critical power cycle. *Chin. J. Chem. Eng.* **2015**, *23*, 572–577. [[CrossRef](#)]
25. Sánchez, C.J.N.; Da Silva, A.K. Technical and environmental analysis of trans-critical Rankine cycles operating with numerous CO₂ mixtures. *Energy* **2018**, *142*, 180–190. [[CrossRef](#)]
26. Xia, J.; Wang, J.; Zhang, G.; Lou, J.; Zhao, P.; Dai, Y. Thermo-economic analysis and comparative study of trans-critical power cycles using CO₂-based mixtures as working fluids. *Appl. Therm. Eng.* **2018**, *144*, 31–44. [[CrossRef](#)]
27. Guo, J.; Li, M.; He, Y.; Xu, J. A study of new method and comprehensive evaluation on the improved performance of solar power tower plant with the CO₂-based mixture cycles. *Appl. Energy* **2019**, *256*, 113837. [[CrossRef](#)]
28. Pan, L.; Ma, Y.; Li, T.; Li, H.; Li, B.; Wei, X. Investigation on the cycle performance and the combustion characteristic of two CO₂-based binary mixtures for the trans-critical power cycle. *Energy* **2019**, *179*, 454–463. [[CrossRef](#)]
29. Yu, H.; Lu, X.; Zhang, W.; Liu, J. A Theoretical Study on the Thermal Performance of an Increasing Pressure Endothermic Cycle for Geothermal Power Generation. *Energies* **2024**, *17*, 1031. [[CrossRef](#)]
30. Lemmon, E.W.; Bell, I.H.; Huber, M.L.; McLinden, M.O. *NIST Standard Reference Database 23: Reference Fluid Thermodynamic and Transport Properties-REFPROP*; Version 10.0; National Institute of Standards and Technology; Standard Reference Data Program: Gaithersburg, MD, USA, 2018. [[CrossRef](#)]
31. Wu, C.; Wang, S.; Jiang, X.; Li, J. Thermodynamic analysis and performance optimization of transcritical power cycles using CO₂-based binary zeotropic mixtures as working fluids for geothermal power plants. *Appl. Therm. Eng.* **2017**, *115*, 292–304. [[CrossRef](#)]
32. Wang, Z.; Hu, Y.; Xia, X.; Zuo, Q.; Zhao, B.; Li, Z. Thermo-economic selection criteria of working fluid used in dual-loop ORC for engine waste heat recovery by multi-objective optimization. *Energy* **2020**, *197*, 117053. [[CrossRef](#)]
33. Abas, N.; Kalair, A.R.; Khan, N. Natural and synthetic refrigerants, global warming: A review. *Renew. Sustain. Energy Rev.* **2018**, *90*, 557–569. [[CrossRef](#)]
34. Hasan, A.R.; Kabir, C.S.; Sarica, C. *Fluid Flow and Heat Transfer in Wellbores*; Society of Petroleum Engineers: Richardson, TX, USA, 2002.
35. Wang, Z.; Sun, B.; Wang, J.; Hou, L. Experimental study on the friction coefficient of supercritical carbon dioxide in pipes. *Int. J. Greenh. Gas Control* **2014**, *25*, 151–161. [[CrossRef](#)]
36. Hasan, A.R.; Kabir, C.S. A mechanistic model for computing fluid temperature profiles in gas-lift wells. *SPE Prod. Facil.* **1996**, *11*, 179–185. [[CrossRef](#)]

Disclaimer/Publisher’s Note: The statements, opinions and data contained in all publications are solely those of the individual author(s) and contributor(s) and not of MDPI and/or the editor(s). MDPI and/or the editor(s) disclaim responsibility for any injury to people or property resulting from any ideas, methods, instructions or products referred to in the content.